remote sensing

Article

FY-4A/AGRI Aerosol Optical Depth Retrieval Capability Test and Validation Based on NNAeroG

Haonan Ding [1,2,†], Limin Zhao [2,†], Shanwei Liu [1], Xingfeng Chen [2,*], Gerrit de Leeuw [2,3], Fu Wang [4,5], Fengjie Zheng [6], Yuhuan Zhang [7], Jun Liu [2], Jiaguo Li [2], Lu She [8], Yidan Si [4] and Xingfa Gu [2,9,10]

1 College of Oceanography and Space Informatics, China University of Petroleum (East China), Qingdao 266580, China
2 Aerospace Information Research Institute, Chinese Academy of Sciences, Beijing 100094, China
3 KNMI (Royal Netherlands Meteorological Institute), 3730 AE De Bilt, The Netherlands
4 State Key Laboratory of Severe Weather, Chinese Academy of Meteorological Sciences, Beijing 100081, China
5 CMA Earth System Modeling and Prediction Centre (CEMC), Beijing 100081, China
6 School of Space Information, Space Engineering University, Beijing 101416, China
7 Satellite Application Center for Ecology and Environment, Ministry of Ecology and Environment of the People's Republic of China, Beijing 100094, China
8 College of Resources and Environmental Science, Ningxia University, Yinchuan 750021, China
9 University of Chinese Academy of Sciences, Beijing 100049, China
10 School of Remote Sensing and Information Engineering, North China Institute of Aerospace Engineering, Langfang 065000, China
* Correspondence: chenxf@aircas.ac.cn
† These authors contributed equally to this work.

Citation: Ding, H.; Zhao, L.; Liu, S.; Chen, X.; de Leeuw, G.; Wang, F.; Zheng, F.; Zhang, Y.; Liu, J.; Li, J.; et al. FY-4A/AGRI Aerosol Optical Depth Retrieval Capability Test and Validation Based on NNAeroG. *Remote Sens.* **2022**, *14*, 5591. https://doi.org/10.3390/rs14215591

Academic Editor: Carmine Serio

Received: 6 September 2022
Accepted: 3 November 2022
Published: 5 November 2022

Abstract: The Advanced Geostationary Radiation Imager (AGRI) is one of the main imaging sensors on the Fengyun-4A (FY-4A) satellite. Due to the combination of high spatial and temporal resolution, the AGRI is suitable for continuously monitoring atmospheric aerosol. Existing studies only perform AOD retrieval on the dark target area of FY-4A/AGRI, and the full disk AOD retrieval is still under exploration. The Neural Network AEROsol Retrieval for Geostationary Satellite (NNAeroG) based on the Fully Connected Neural Network (FCNN) was used to retrieve FY-4A/AGRI full disk aerosol optical depth (AOD). The data from 111 ground-based Aerosol Robotic Network (AERONET) and Sun–Sky Radiometer Observation Network (SONET) sites were used to train the neural network, and the data from 28 other sites were used for independent validation. FY-4A/AGRI AOD data from 2017 to 2020 were validated over the full disk and three different surface types (vegetated areas, arid areas, and marine and coastal areas). For general validation, the AOD predicted by the application of NNAeroG to FY-4A/AGRI observations is consistent with the ground-based reference AOD data. The validation of the FY-4A/AGRI AOD versus the reference data set shows that the root-mean-square error (RMSE), mean absolute error (MAE), R squared (R^2), and percentage of data with errors within the expected error ± (0.05 + 15%) (EE15) are 0.237, 0.145, 0.733, and 58.7%, respectively. The AOD retrieval accuracy over vegetated areas is high but there is potential for improvement of the results over arid areas and marine and coastal areas. AOD retrieval results of FY-4A/AGRI were compared under fine and coarse modes. The retrieved AOD has low accuracy in coarse mode but is better in coarse–fine mixed mode and fine mode. The current AOD products over the ocean of NNAeroG-FY4A/AGRI are not recommended. Further development of algorithms for marine areas is expected to improve the full disk AOD retrieval accuracy.

Keywords: aerosol optical depth (AOD); FY-4A/AGRI; geostationary satellite; neural network

1. Introduction

Atmospheric aerosols are heterogeneous systems composed of solid and liquid particles suspended in the atmosphere [1]. Aerosols play an important role in the Earth's radiation balance, hydrological cycle, and biogeochemical cycles [2]. They are also important for human health, especially for people with respiratory problems and lung diseases [3]. Therefore, it is important to obtain accurate information on the occurrence of aerosols and their properties. There are four main ways to monitor aerosols: ground-based measurements [4–7], airborne measurements [8,9], observations using polar-orbiting satellites [10–12], and observations using geostationary satellites [13,14]. The primary parameter obtained from satellite observations is the aerosol optical depth (AOD), i.e., the vertical integral of the aerosol extinction from the surface to the top of the atmosphere (TOA) [15–17]. AOD is an important optical parameter for characterizing atmospheric aerosol properties and spatial distribution. Geostationary satellites provide aerosol observations with high temporal resolution over a large area determined by the satellite's location, which allows for the frequent monitoring of the same location on the ground. The observation frequency of geostationary satellites can reach the level of hours or even minutes, which has obvious advantages for monitoring aerosols.

AOD is retrieved from satellite observations using a variety of methods, depending on the sensor characteristics and the retrieval approach chosen [18]. Here, we briefly summarize aerosol retrieval methods developed for geostationary satellites. The current Advanced Himawari Imager (AHI) official aerosol product is retrieved using a deep-blue (DB)-type method [19]. Ge et al. (2019) [20] proposed a new normalized difference vegetation index (NDVI) for the AHI sensor for an improved surface reflectance estimation for the application of the dark target (DT) retrieval method. The AOD results between AHI retrieval and ground-based data show good agreements with an R^2 of 0.81. Li et al. (2020) [21] used an improved time series algorithm (ITS) to retrieve the AHI AOD over eastern China and the results had good agreement with the reference AOD data at eleven sun photometer sites. Wang et al. (2020) [22] used linear regression to build relationships between the surface reflectances in the visible and shortwave infrared (SWIR) bands, which were used to retrieve the AHI AOD using a radiative transfer model. She et al. (2020) [23] developed deep neural network (DNN) models to retrieve AOD from the Himawari-8 full disk TOA reflectance and achieved an accuracy that is better than that of the official Japan Aerospace Exploration Agency (JAXA) product. Chen et al. (2022) [24] proposed a neural network aerosol retrieval for geostationary satellite (NNAeroG) for AOD retrieval using AHI data and the results were significantly better than the official JAXA aerosol products, with 63.7% of the AOD data being within the expected error of $\pm$ (0.05 + 15%) (EE15). Jiang et al. (2021) [25] developed a new algorithm for retrieval of AOD over land using Fengyun-4A/Advanced Geostationary Radiation Imager (FY-4A)/(AGRI) data. MCD43C2 data sets were used to obtain the band surface reflectance and establish a surface reflectance ratio database. Then, the Second Simulation of a Satellite Signal in the Solar Spectrum Vector (6SV) model was used to build lookup tables (LUT) used in the retrieval of hourly AOD. Xie et al. (2022) [26] proposed an FY-4A/AGRI AOD retrieval algorithm called the multichannel (MC) algorithm, which was applied to aerosol retrieval in South Asia. The percentage of AOD data obtained by the application of this algorithm to FY-4A/AGRI data within EE15 was 63.71%. There are few studies on FY-4A/AGRI AOD. The full disk FY-4A/AGRI AOD has thus far not been retrieved and thus no official FY-4A/AGRI AOD product is available. This paper aims to investigate whether enough information is available from FY-4A/AGRI observations to retrieve AOD using the NNAeroG method.

In contrast to sun-synchronous satellites, a geostationary satellite such as FY-4A provides multiple observations each day over the same location, which can be used in time series algorithms [27]. We used the reflections measured in spectral bands at wavelengths in the visible, near-infrared (VNIR) and SWIR parts of the solar spectrum. Additionally, NDVI was also used as input information because the full disk area includes a variety of surface types over land, coastal water and open ocean. Additionally, the aerosol types vary substantially within the disk area, as well as meteorological and climatic conditions. In order to constrain the retrieval, information from both spatial measurements over a large area and time sequences of such measurements were used. For the neural network training and validation, each data sample includes an input (satellite TOA reflectance in different spectral bands) and output (AOD based on ground data acquisition), which are available from sun photometer measurements provided by the Aerosol Robotic Network (AERONET) [28] and by the Sun–Sky Radiometer Observation Network (SONET) [29]. The aerosol products retrieved by NNAeroG can be used for air quality monitoring and climate research in the FY-4A/AGRI full disk. This article is structured as follows. Section 2 describes the data used in this study and the NNAeroG retrieval algorithm developed for FY-4A/AGRI is introduced in Section 3. Section 4 provides the retrieval results, validation results, and corresponding analyses. The FY-4A/AGRI High Temporary Resolution AOD product obtained from NNAeroG and the comparison with the AOD results of Himawari-8/AHI are discussed in Section 5. Conclusions are presented in Section 6 where we also discuss the limitations of this work and the next steps.

2. Materials

2.1. FY-4A/AGRI Data

FY-4A is the first of China's second-generation geostationary meteorological satellites operated by the National Satellite Meteorological Center (NSMC) of the China Meteorological Administration (CMA), Beijing, China [30]. FY-4A was launched on 11 December 2016, in a geostationary orbit at 104.7°E and has been operational as a weather satellite since 25 September 2017. Three-axis stable attitude control was adopted by FY-4A, which significantly improved the efficiency of earth observation and can effectively observe the disastrous weather process in real-time [31]. It is equipped with AGRI, a Geostationary Interferometric Infrared Sounder (GIIRS), a Lightning Mapping Imager (LMI) and a Space Environment Package (SEP) [32]. FY-4A/AGRI data and its data format description can be downloaded from the NSMC website (http://satellite.nsmc.org.cn, last access 7 June 2022). The observation time interval of the full disk observation mode is about 15 min. This means that AGRI can image full disk 40 times a day [33].

In this study, the full disk FY-4A/AGRI Level 1 radiance data and the GEO positioning data (single file) with a spatial resolution of 4 km from 2017 to 2020 were used, which was processed in a series of steps such as radiometric calibration of FY-4A/AGRI Level 0 source package data. Since only the clear sky observation data of FY-4A/AGRI can be used to retrieve AOD, the 4 km resolution full disk cloud mask (CLM) product is used to select cloud-free pixels. The cloud data are provided in NetCDF format and discriminate between cloud, probable cloud, probable clear, clear and other types.

The FY-4A/AGRI provides observations in 14 wavebands that are sampled at a nominal 0.5/1 km spatial resolution at nadir in the VIS and NIR, 2 km in the SWIR, and 4 km in the TIR spectral bands [30]. The spectral bands cover wavelengths from 0.45 to 13.8 µm as shown in Table 1. The onboard radiometric calibration accuracy is 0.5 K and the sensitivity is 0.2 K [34].

2.2. Ground-Based Data

2.2.1. AERONET Data

AERONET is a global network of sun–sky photometers providing near-continuous daytime measurements of spectral solar irradiance, spectral AOD, water vapor, and inversion aerosol products [28]. AERONET sites provide long-term spectral AOD at discrete wavelengths ranging from the visible to the NIR (340–1020 nm). The estimated uncertainty of the AERONET AOD is about 0.01–0.02 and one sigma uncertainty of 0.02 is commonly used as a reference for satellite AOD product validation [35,36]. The AERONET data are categorized into three different quality levels: L1.0 (unscreened), L1.5 (cloud-screened), and L2.0 (cloud-screened and quality-assured). In this study, AOD data at 440 nm, 500 nm and 675 nm with quality Level 1.5 from the latest Version 3.0 were used (https://aeronet.gsfc.nasa.gov, last access 7 June 2022). All AERONET Version 3.0 data from the 123 AERONET sites between 24°E–174°E and 70°N–40°S during 2017–2020 were used for training (98 sites) and validation (25 sites which were not used for training). The area covers most of Asia and Australia, as well as parts of Europe and Africa (Figure 1). It covers vegetated areas, arid areas, and marine and coastal areas. The information and characteristics of AERONET validation sites are shown in Table 2.

Table 1. FY-4A AGRI band characteristics.

Band Notation	Band	Central Wavelength (nm)	Spatial Resolution (km)
VIS	1	0.45~0.49	1
	2	0.55~0.75	0.5~1
NIR	3	0.75~0.90	1
Cirrus	4	1.36~1.39	2
SWIR	5	1.58~1.64	2
	6	2.1~2.35	2~4
	7	3.5~4.0	2
	8	3.5~4.0	4
Water Vapor	9	5.8~6.7	4
	10	6.9~7.3	4
TIR	11	8.0~9.0	4
	12	10.3~11.3	4
	13	11.5~12.5	4
	14	13.2~13.8	4

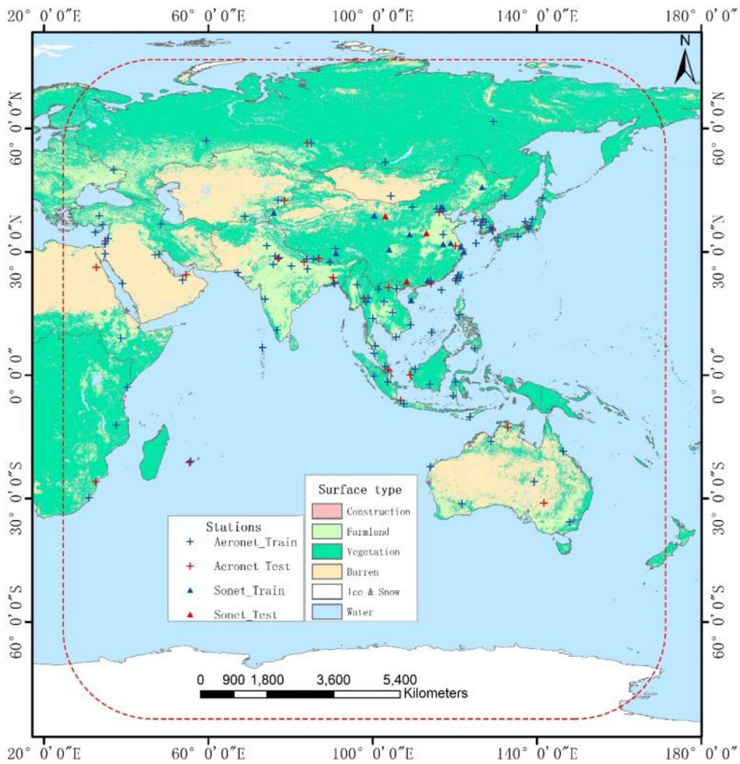

Figure 1. Map showing the area covered by the FY-4A/AGRI full disk (red box: 24°E–174°E and 80°N–80°S), with surface type indicated in color as shown in the legend. Additionally shown are the locations of the AERONET sites (crosses), 123 in total, and the SONET sites (triangles), 16 in total. Blue symbols indicate the sites used for training the neural network, 111 in total, and red symbols indicate the validation sites, 28 in total. The station locations include most surface type areas. Surface type data are obtained from the Food and Agriculture Organization of the United Nations (FAO) (https://data.apps.fao.org/map/catalog/srv/eng/catalog.search#/home, last access 7 June 2022).

Table 2. AERONET sites used to verify the NNAeroG only for validation which were not used for training.

Site Name	Position	Purpose	Characteristics
UEM_Maputo	25.950°S, 32.599°E	Validation	marine and coastal
Qena_SVU	26.2°N, 32.747°E	Validation	arid
Tel-Aviv_University	32.113°N, 34.806°E	Validation	marine and coastal
Maido_OPAR	21.08°S, 55.383°E	Validation	marine and coastal
Tomsk_22	56.417°N, 84.074°E	Validation	vegetated
Masdar_Institute_2	24.442°N, 54.617°E	Validation	marine and coastal
IAOCA-KRSU	42.464°N, 78.529°E	Validation	arid
Lumbini	27.49°N, 83.28°E	Validation	arid
Doi_Inthanon	18.59°N, 98.486°E	Validation	vegetated
Pioneer_JC	1.384°N, 103.755°E	Validation	marine and coastal
BMKG_Jakarta	6.155°S, 106.841°E	Validation	marine and coastal
Fowlers_Gap	31.086°S, 141.701°E	Validation	arid
Jabiru	12.661°S, 132.893°E	Validation	marine and coastal
Pontianak	0.075°N, 109.191°E	Validation	marine and coastal
DRAGON_Minowa	35.915°N, 137.981°E	Validation	vegetated
KORUS_UNIST_Ulsan	35.582°N, 129.19°E	Validation	vegetated
Seoul_SNU	37.458°N, 126.951°E	Validation	vegetated
Chiayi	23.496°N, 120.496°E	Validation	marine and coastal
QOMS_CAS	28.365°N, 86.948°E	Validation	arid
Beijing-CAMS	39.933°N, 116.317°E	Validation	vegetated
Hong_Kong_PolyU	22.303°N, 114.18°E	Validation	marine and coastal
Taihu	31.421°N, 120.215°E	Validation	marine and coastal
Son_La	21.332°N, 103.905°E	Validation	vegetated
Amity_Univ_Gurgaon	28.317°N, 76.916°E	Validation	vegetated
Dhaka_University	23.728°N, 90.398°E	Validation	marine and coastal

2.2.2. SONET Data

SONET is a ground-based sun–sky photometer network, established and maintained by the Institute of Remote Sensing and Digital Earth, Chinese Academy of Sciences [37]. SONET utilizes the standard CIMEL CE318 sun–sky radiometer to acquire dozens of aerosol properties. The average AOD difference (0.002 ± 0.001) between SONET and AERONET is much smaller than the AERONET AOD uncertainty. While the calibration difference is minimized in SONET by employing master instruments directly calibrated by AERONET/PHOTONS. This suggests that not only are the two networks comparable, but the accuracies of both networks are also quite high [29]. The multiwavelength polarization measurement capability of these networks can provide long-term columnar atmospheric aerosol properties over China [38]. In view of the sparsity of AERONET sites in China, SONET provides a supplementary source for sun photometer data. In this study, we jointly use AERONET and SONET to select training and validation across China. The definitions of SONET follow the AERONET data level protocols (version 2). All L1.5 (cloud-screened) data from the 16 SONET sites between 75°E–130°E and 18°N–46°N during 2017–2019 were used for training and validation (www.sonet.ac.cn, last access 7 June 2022). Information on the SONET sites is presented in Table 3.

2.3. Study Area

The study area is the area observed by the FY-4A/AGRI full disk between 24°E–174°E and 80°N–80°S, as shown in Figure 1. Figure 1 also shows the locations of the AERONET and SONET sites used for training and validation. The area covers most of Eurasia, Australia, also part of Africa, the Arctic and Antarctica.

Table 3. SONET sites used to train and verify the NNAeroG.

Site Name	Position	Purpose	Characteristics
Sanya	18.29°N, 109.379°E	Training	marine and coastal
Guangzhou	23.069°N, 113.381°E	Training	marine and coastal
Yanqihu	40.408°N, 116.674°E	Training	marine and coastal
Shanghai	31.284°N, 121.481°E	Training	marine and coastal
Zhoushan	29.994°N, 122.19°E	Training	marine and coastal
Harbin	45.705°N, 126.614°E	Training	vegetation
Chengdu	30.584°N, 104.989°E	Training	vegetation
Xian	34.223°N, 109.001°E	Training	arid
Nanjing	32.115°N, 118.957°E	Training	vegetation
Hefei	31.905°N, 117.162°E	Training	vegetation
Zhangye	38.854°N, 100.364°E	Training	arid
Kashi	39.504°N, 75.93°E	Training	arid
Lhasa	29.648°N, 91.088°E	Training	arid
Minqin	38.633°N, 103.089°E	Validation	arid
Songshan	34.535°N, 113.096°E	Validation	vegetation
Nanning	22.839°N, 108.285°E	Validation	vegetation

3. Method

3.1. Strategy and Data Set Preprocessing

The procedure of FY-4A/AGRI AOD retrieval is based on the NNAeroG algorithm as that for Himawari-8/AHI [24]. However, the feature selection obtained for the AGRI bands is through Random Forest (RF) whereas AHI used the XGBoost machine learning method. Furthermore, in this study, NDVI was used for training the network. This is a parameter that NNAeroG has not used before. The flow chart of the modified NNAeroG used in this study is shown in Figure 2.

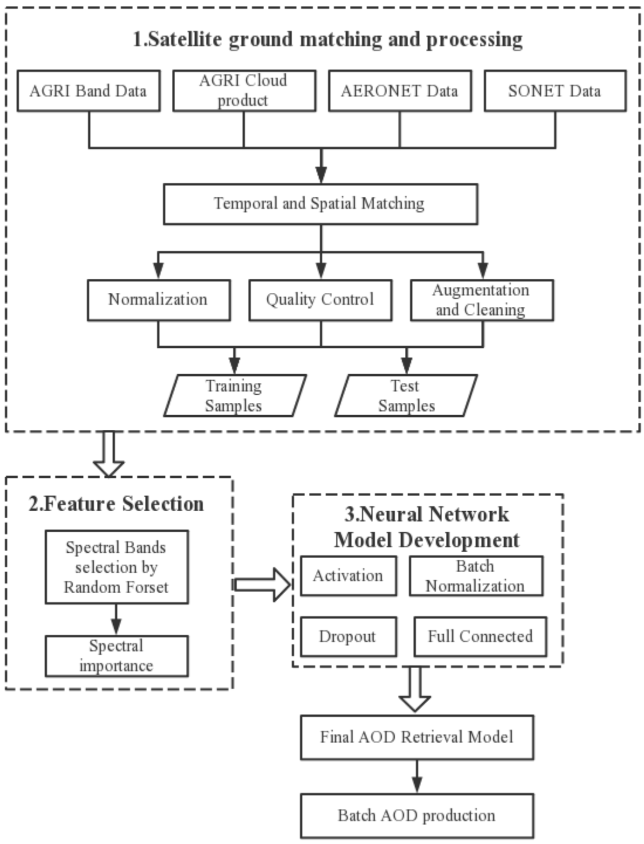

Figure 2. Flow chart of NNAeroG training and validation, modulated for FY-4A/AGRI AOD estimation.

In the first step, AGRI band data, the CLM product, AERONET data and SONET data were collocated in space and time. AERONET AOD at 550 nm wavelength (AOD550) was obtained from interpolation of the AODs in the 440 nm, 500 nm and 675 nm bands, using the quadratic polynomial method. The mean values of AOD over ±30 min from the satellite imaging time were extracted to match the satellite data at the same location. The Earth's surface albedo measured at TOA in bands 1–6 and the brightness temperatures measured at TOA in bands 7–14 were obtained by radiometric calibration of FY-4A/AGRI data. We calculated the reflectances from the albedo in bands 1–6 using:

$$\rho_\lambda = \frac{\pi L D^2}{ESUN_\lambda \cos(\theta)'} \tag{1}$$

where ρ_λ is the TOA reflectance at wavelength λ; L is the TOA radiance after radiometric calibration; D is the astronomical distance from the Sun to the Earth; θ is the zenith angle of the Sun; and $ESUN_\lambda$ is the solar spectral irradiance at the upper boundary of the atmosphere with the central wavelength of λ.

After temporal and spatial matching, satellite ground-matching samples were normalized and quality controlled. The Solar azimuth angle (*SOA*), satellite azimuth angle (*SAA*) and Relative Azimuth Angle (*REA*) were also used to quality control and calculate the value of reflectance. *REA* was defined by:

$$REA = |SOZ - SAZ|, \tag{2}$$

where *SOZ* is the Solar zenith angle and *SAZ* is the satellite zenith angle.

There were fewer samples with AOD > 1.3, which would lead to a lack of learning for high AOD values. Therefore, these samples were copied and augmented by adding 2% Gaussian noise [24]. The samples were divided into two parts, training and validation, to ensure that the validation samples were independent of the training samples.

In the second step, multi-spectral and multi-pixel (sub-image centered on the site) geostationary data were combined in one sample, which is an important feature for aerosol retrieval. The decision-based RF machine learning method can provide the importance value of each input feature.

In the third step, to establish a machine learning model, the neural network is recommended for its excellent non-linear fitting ability [39]. The state-of-the-art practices of Fully Connected Neural Network (FCNN) training were used. The mini-batch gradient descent search method was used with a batch size of 200 epochs to ensure a stable and robust solution. Through selection of activation function selection, batch normalization, drop processing and full connection network parameters setting, the final model for FY-4A/AGRI AOD estimation was established with multiple iterations.

Finally, the FCNN was trained, tested and fixed. Temporal and spatial information were selected according to the test results of the FCNN model. AOD over the FY-4A/AGRI full disk was predicted, and the fixed FCNN model was ready to be used to retrieve aerosol with a large amount of remote sensing data.

3.2. Fully Connected Neural Network (FCNN)

Different machine learning methods were tested and the FCNN was selected for NNAeroG because it demonstrated the best performance. For the TOA, measurements are organized as a vector, not as an image. For every pixel, the FCNN could meet the input format. The FCNN (one input, one hidden, and one output layer) architecture for NNAeroG was designed as shown in Figure 3.

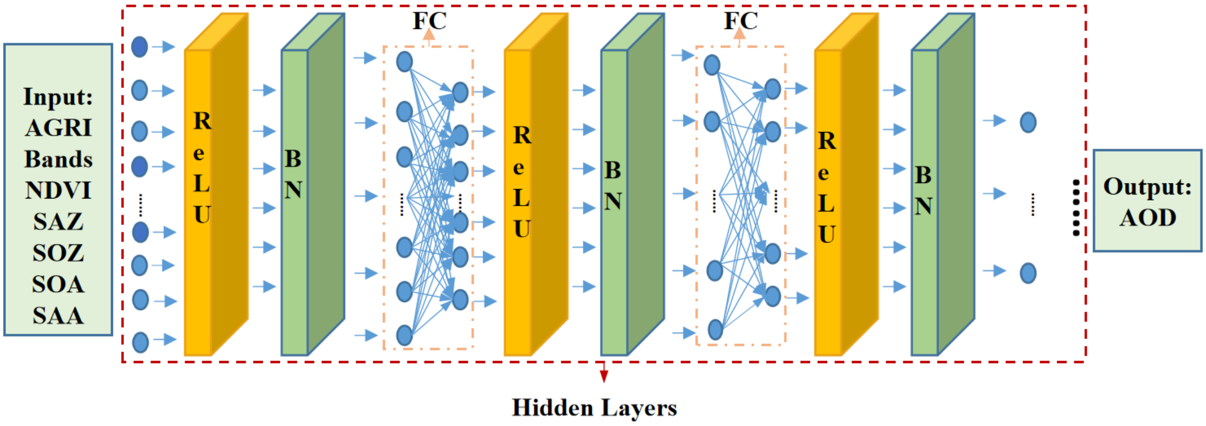

Figure 3. Architecture of the FCNN model for FY-4A/AGRI aerosol retrieval (input nodes: feature selection of AGRI bands (b1, b2, b3, b5, b6, b7, b8, b9, b10, b11, b13), SAZ, SOA, SAA, SOZ, and the NDVI; output node: AOD at 550 nm). Rectified linear unit (ReLU) is the activation layer. BN is a batch normalization layer and was adopted to perform the standardizing and normalizing operations on the input of a layer coming from a previous layer, by bringing the numerical data to a common scale. DP is the dropout layer, which was used to reduce overfitting by randomly and temporarily deleting neurons in the hidden layer during the training with a given probability. FC is the fully connected layer. The circles represent the input and output parameter of one layer, the arrows represent the transfer direction of FCNN.

In this study, the ReLU nonlinear function was used:

$$f(z) = \max(z, 0), \tag{3}$$

where z is a linear combination of all previous layer neuron values with multiple weights and one bias and *f(z)* is the output neuron. The ReLU nonlinear function makes a deeper neural network more feasible to train than other non-linear functions such as the sigmoidal function used in the three-layer FCNN [40].

In the fully connected layer, the basic unit is the neuron, which is a weighted summation of its inputs. The output of a neuron is expressed as:

$$v = \sum_{i=1}^{m} \omega_i * x_i, \tag{4}$$

where ω_i is the weighting coefficient for the input x_i. The training process is performed to obtain the best ω_i for achieving the best prediction accuracy.

3.3. Training Configurations and Model Validation

Before training, the loss function, activation function and optimizer should be configured. In each training with a sample, the loss function was used to evaluate the fitting performance by comparing the output in the training data set and the FCNN was used to predict output. Four parameters were used as metrics to evaluate the performance of the method: (i) root mean square error (RMSE) (Equation (5)); (ii) mean absolute error (MAE) (Equation (6)); (iii) R squared (R^2) (Equation (7)); (iv) the percentage of NNAeroG retrievals falling within EE15, which were applied to MODIS and Himawari-8/AHI data over land and was adopted by others [41,42].

$$\text{RMSE} = \sqrt{\frac{1}{n}\sum_{i=1}^{n}\left(y_{ti} - y_{pi}\right)^2}, \tag{5}$$

$$\text{MAE} = \frac{1}{n}\sum_{i=1}^{n}\left|y_{ti} - y_{pi}\right|, \tag{6}$$

$$R^2 = 1 - \frac{\frac{1}{n}\sum_{i=1}^{n}\left(y_{pi} - y_{ti}\right)^2}{\frac{1}{n}\sum_{i=1}^{n}\left(y_i - y_{ti}\right)^2}, \quad (7)$$

where y_{ti} is the training data set; y_{pi} is the predicted data set; y_i is the mean of y_{ti}; and n is the total number of samples.

4. Results

4.1. General Validation

The NNAeroG was trained and its performance was validated by comparison with the data from the AERONET and SONET data set aside for validation. The full disk validation results are presented in Figure 4. Figure 4 shows that 58.7% of the AOD retrieved using the training data are within EE15, the RMSE, MAE and R^2 are 0.237, 0.145 and 0.733, respectively. The above and below EE are similar. However, the slope is <1 and the figure shows that the larger AOD is underestimated by NNAeroG.

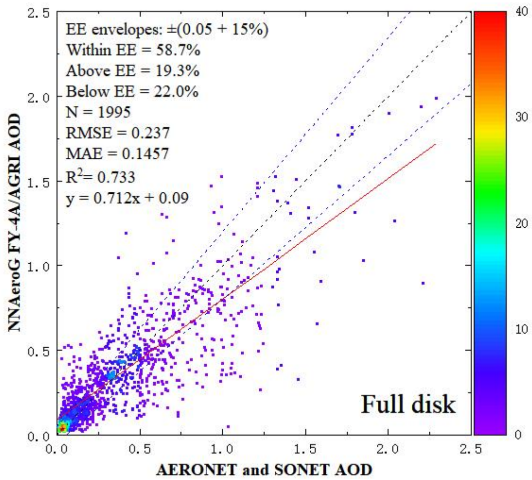

Figure 4. Scatterplots of FY-4A/AGRI retrieved full disk AOD versus AERONET and SONET reference data. The blue lines are the EE envelopes for AOD of ± (0.05 + 15%). The red line is the linear fitting line of AOD. The black line represents the 1:1 line.

A comparison of the full disk AOD retrieval results with Himawari-8/AHI AOD validation results published by She et al. (2020) [23], Chen et al. (2022) [24] and the official product from JAXA is presented in Table 4. Compared with the official (JAXA) AHI AOD product, the R^2 for NNAeroG is 0.4 larger and RMSE is smaller by 0.141, which shows that the NNAeroG results are a significant improvement over those from the official AHI algorithm. Compared with the AHI AOD retrieval results presented by She et al. (2020) [23], the FY-4A/AGRI full disk AOD retrieval using NNAeroG, RMSE is smaller by 0.056, R^2 is larger by 0.003, and the overall accuracy is also smaller. The AHI AOD retrieved using the NNAeroG algorithm is better than AGRI in all aspects because Himawari-8/AHI has more infrared bands with a higher spatial resolution than FY-4A/AGRI, especially a visible band at 0.51 for true color image synthesis [43]. In the infrared bands, the spatial resolution of AHI is 2 km while that of FY-4A/AGRI is 4 km, indicating that FY-4A/AGRI still has a certain disadvantage in detecting fine-scale surface and cloud detail compared with AHI [44].

4.2. AOD Results of Different Surface Types

Aerosol retrieval over land surface requires a separation of the TOA reflectance due to aerosol particles and that due to surface reflectance. This is best achieved over a dark surface, which contributes little to the TOA reflectance which is mainly due to atmospheric contributions from which the aerosol contribution can be determined with high accuracy. Over brighter surfaces, aerosol retrieval is less accurate. In order to investigate the effect of the underlying surface on the aerosol retrieval results, the NDVI was used to discriminate between dark vegetated areas (AOD accuracy is high in theory) and brighter arid areas (with little or no vegetation, which would lead to relatively weak atmospheric signals and low AOD accuracy in theory). The third surface type considered is coastal water near the sea–land boundary which, in contrast to the open ocean (type 1 water which is dark), is brighter due to suspended matter over which significant retrieval errors are encountered. The AERONET and SONET reference data were divided into three categories according to the surface type at each site: vegetated areas (including seasonal vegetation areas), arid areas, and marine–coastal areas.

Table 4. Overview of published validation studies of AOD in full disk for different methods applied to multi-spectral sensors and NNAeroG for different multi-spectral sensors.

Method	Literature	Sensor	RMSE	MAE	R^2	% In EE	Study Area
DNN	She et al. [23]	AHI	0.172	—	0.730	—	Full disk
JAXA	She et al. [23]	AHI	0.378	—	0.333	—	Full disk
NNAeroG	Chen et al. [24]	AHI	0.124	0.092	0.859	58.7%	China
NNAeroG	This paper	AGRI	0.237	0.145	0.733	63.7%	Full disk

4.2.1. Vegetated Areas

Vegetated areas have dark surfaces and the TOA signal is governed by the atmospheric contribution. The comparison of the retrieved AOD with reference data over the vegetated areas is shown in Figure 5.

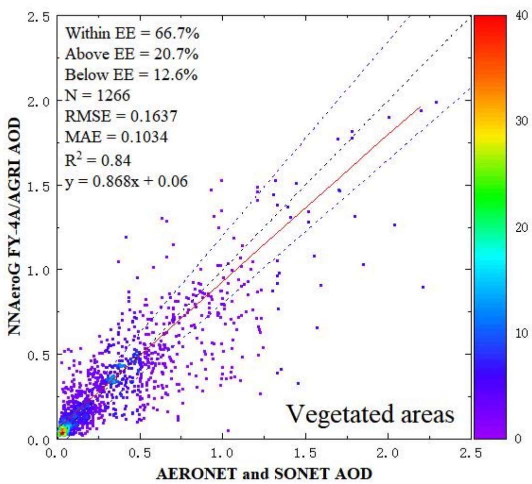

Figure 5. Scatterplots of FY-4A/AGRI retrieved AOD versus AERONET and SONET reference data over vegetated areas. The blue lines are the EE envelopes for AOD of ± (0.05 + 15%). The red line is the linear fitting line of AOD. The black line represents the 1:1 line.

Figure 5 shows that the retrieval accuracy is high for AOD < 0.3 but for higher AOD, the FY-4A/AGRI results are underestimated, as also observed for the full disk results in Figure 4. The comparison of the results for FY-4A/AGRI AOD using NNAeroG over vegetated areas with other published results using other methods is presented in Table 5.

Table 5. Overview of published AOD validation studies over vegetated areas for different methods applied to FY-4A/AGRI data.

Method	Literature	RMSE	MAE	R^2	% In EE	Study Area
MC	Xie et al. [26]	0.16	0.12	—	63.71%	South Asia
6SV-LUT	Xue et al. [25]	0.31	—	0.64	35.56%	China
NNAeroG	This paper	0.163	0.103	0.84	66.7%	Full disk

Table 5 shows that 66.7% of the AOD retrieved using NNAeroG/AGRI over vegetated surfaces are within EE15, the RMSE, MAE and R^2 are 0.163, 0.103 and 0.84, respectively, which is slightly better than the statistical metrics obtained using the MC method. The accuracy of NNAeroG is better than 6SV-LUT in all aspects. The validation of the AOD retrieved using FY-4A/AGRI data over vegetated areas with the NNAeroG method shows that the quality is sufficient for AOD production.

4.2.2. Arid Areas

The surface reflectance of arid areas is relatively high and distinguishing atmospheric aerosol contributions to the TOA reflectance is difficult [45]. The comparison of FY-4A/AGRI/NNAeroG AOD retrieval results over arid areas with reference AERONET and SONET data is shown in Figure 6. The values of the statistical metrics RMSE, MAE, R2 and EE15 are 0.358, 0.228, 0.539 and 47.6%, respectively. For AOD < 0.3, the retrieval results are in good agreement with the AERONET and SONET data. However, for AOD > 0.5, the majority of the AGRI retrieval results are underestimated. The retrieval of arid areas needs further improvement.

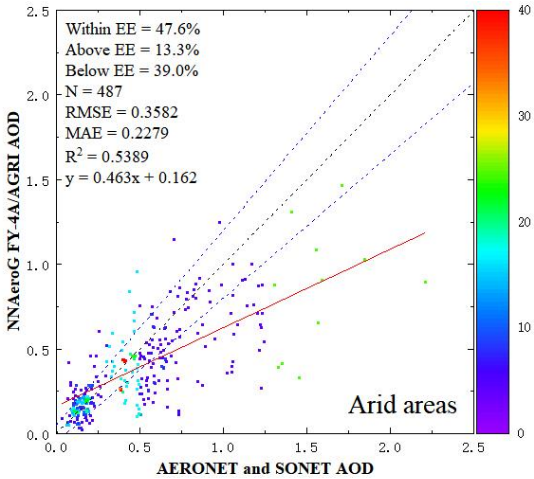

Figure 6. Scatterplots of the AOD retrieved using FY-4A/AGRI over arid areas versus AERONET and SONET reference data. The blue lines are the EE envelopes for AOD of ± (0.05 + 15%). The red line is the linear fitting line of AOD. The black line represents the 1:1 line.

4.2.3. Marine and Coastal Areas

The environmental characteristics of coastal waters are a challenge for aerosol remote sensing. The turbidity of coastal waters, the transition between water and land surface, and the sun glint area have strong spectral and spatial variability leading to poor aerosol retrieval results [46,47]. The retrieval results over marine and coastal areas are shown in Figure 7.

The RMSE, MAE, R^2 and EE15 for the validation of the AOD retrieved over marine and coastal areas are 0.257, 0.201, 0.793 and 38.8%, respectively. The retrieval errors for AOD < 0.1 are generally high with values up to 0.5. For AOD > 0.3, the retrieved AOD is generally low. When the AOD of the ocean-atmosphere is less than 0.1, the satellite does not have enough aerosol optical signals to retrieve the AOD [10]. There are barely any pure marine samples (CE318 sites are located on the land or coast) for our training, therefore the training in marine areas is insufficient. The application of NNAeroG in marine and coastal areas needs much improvement and the method is currently not suitable enough for AOD production. However, this does not mean other algorithms also poorly retrieve AOD of FY-4A/AGRI over the ocean. A Coastal Water AOD retrieval algorithm such as that which was applied on MODIS would achieve high accuracy [47].

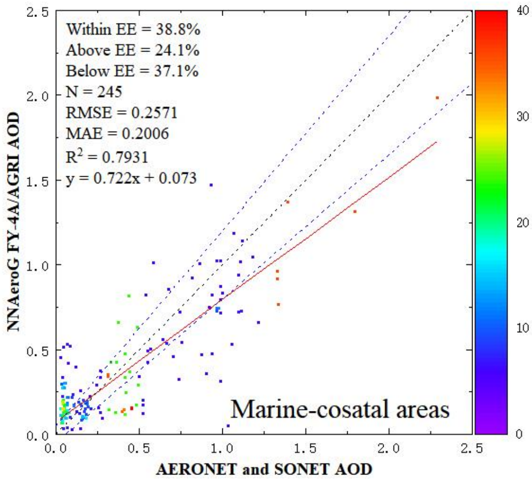

Figure 7. Scatterplots of the AOD retrieved using FY-4A/AGRI data over marine and coastal areas versus AERONET and SONET reference data. The blue lines are the EE envelopes for AOD of ± (0.05 + 15%). The red line is the linear fitting line of AOD. The black line represents the 1:1 line.

4.3. Fine and Coarse Mode AOD

As discussed by Chen et al. [27], NNAeroG can discriminate between the fine and coarse mode AOD fractions. Figure 8 shows the comparisons between the FY-4A/AGRI retrieved fine and coarse mode fractions and those available from the reference data sets.

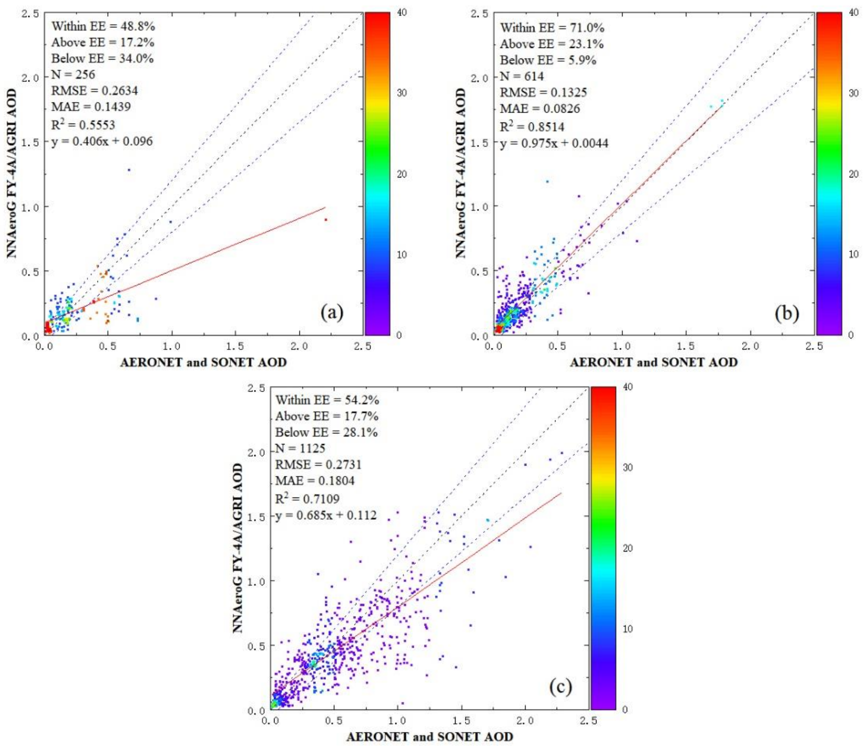

Figure 8. Scatterplots of the fine and coarse mode AOD retrieved using FY-4A/AGRI data versus AERONET and SONET reference data. (**a**) FMF $\leq$ 0.4, (**b**) 0.4 < FMF < 0.7, (**c**) FMF $\geq$ 0.7. The blue lines are the EE envelopes for AOD of ± (0.05 + 15%). The red line is the linear fitting line of AOD. The black line represents the 1:1 line.

Figure 8 shows the validation of the AOD retrieved using FY-4A/AGRI data with the NNAeroG algorithm according to the fine and coarse modes. When FMF $\leq$ 0.4, it belongs to coarse mode and the values of the statistical metrics RMSE, MAE, R^2 and EE15 are 0.263, 0.144, 0.555 and 48.8%, respectively. The coarse mode is mainly composed of sand and dust, which are naturally discharged and mostly occur in arid areas. It is difficult to retrieve when the surface is bright. When 0.4 < FMF < 0.7, the values of the statistical metrics RMSE, MAE, R^2 and EE15 are 0.133, 0.083, 0.851 and 71%, respectively. When FMF $\geq$ 0.7, it belongs to fine mode and the values of the statistical metrics RMSE, MAE, R^2 and EE15 are 0.273, 0.18, 0.711 and 54.2%, respectively. The result is relatively discrete, which may be that the surface is composed of complex surfaces such as artificial buildings and dominated by anthropogenic emissions such as black carbon [27].

5. Discussion

This section generally discusses the FY-4A/AGRI High Temporary Resolution AOD produced by NNAeroG and the comparison with the AOD results of Himawari-8/AHI.

5.1. High Temporal Resolution Products

As an example, Figure 9 shows the spatial distributions of the AGRI-retrieved AOD using the NNAeroG algorithm for the FY-4A/AGRI full disk on 23 April 2020 for every hour from 03:00 to 10:00 UTC. The FY-4A/AGRI AOD spatial distributions are shown as hourly averages. The data clearly show the hour-to-hour variation of the AOD and the different diurnal evolution of the AOD between locations.

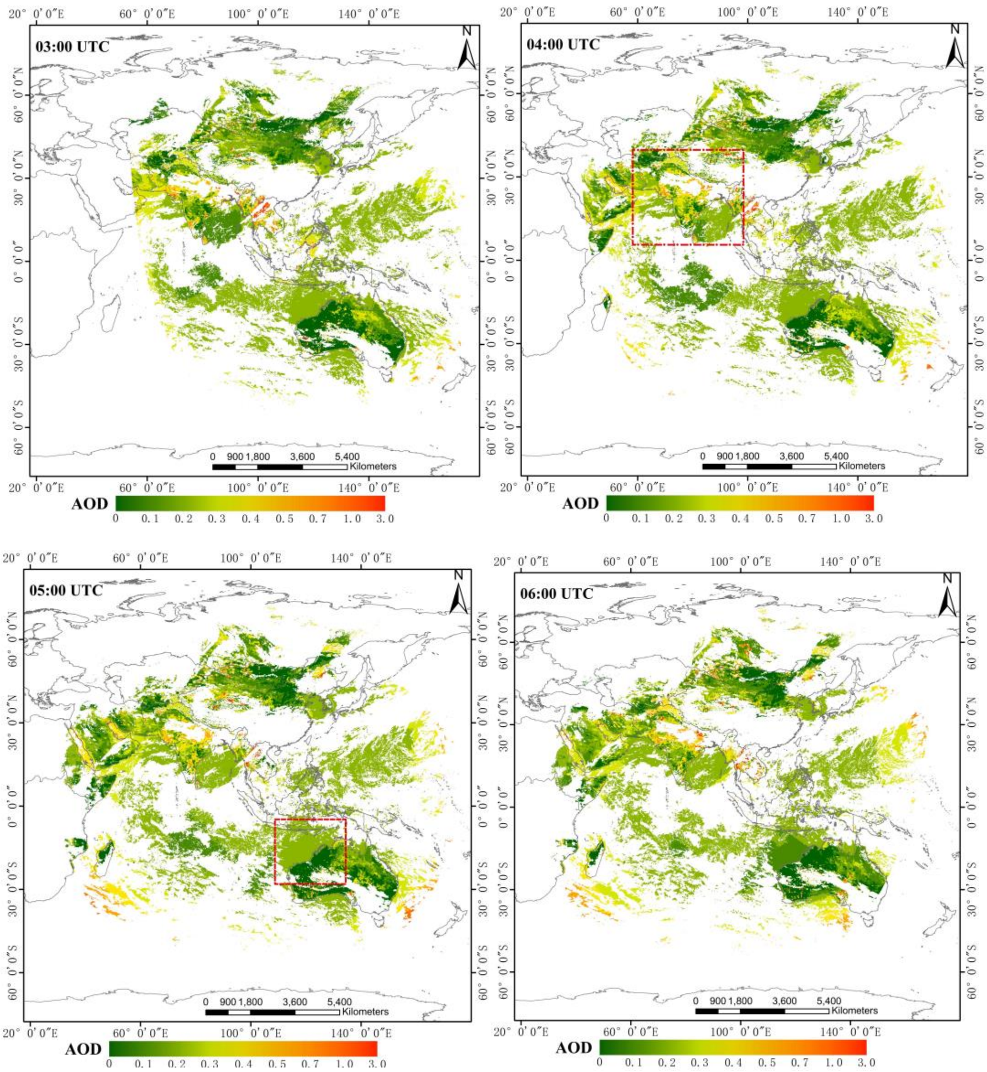

Figure 9. *Cont*.

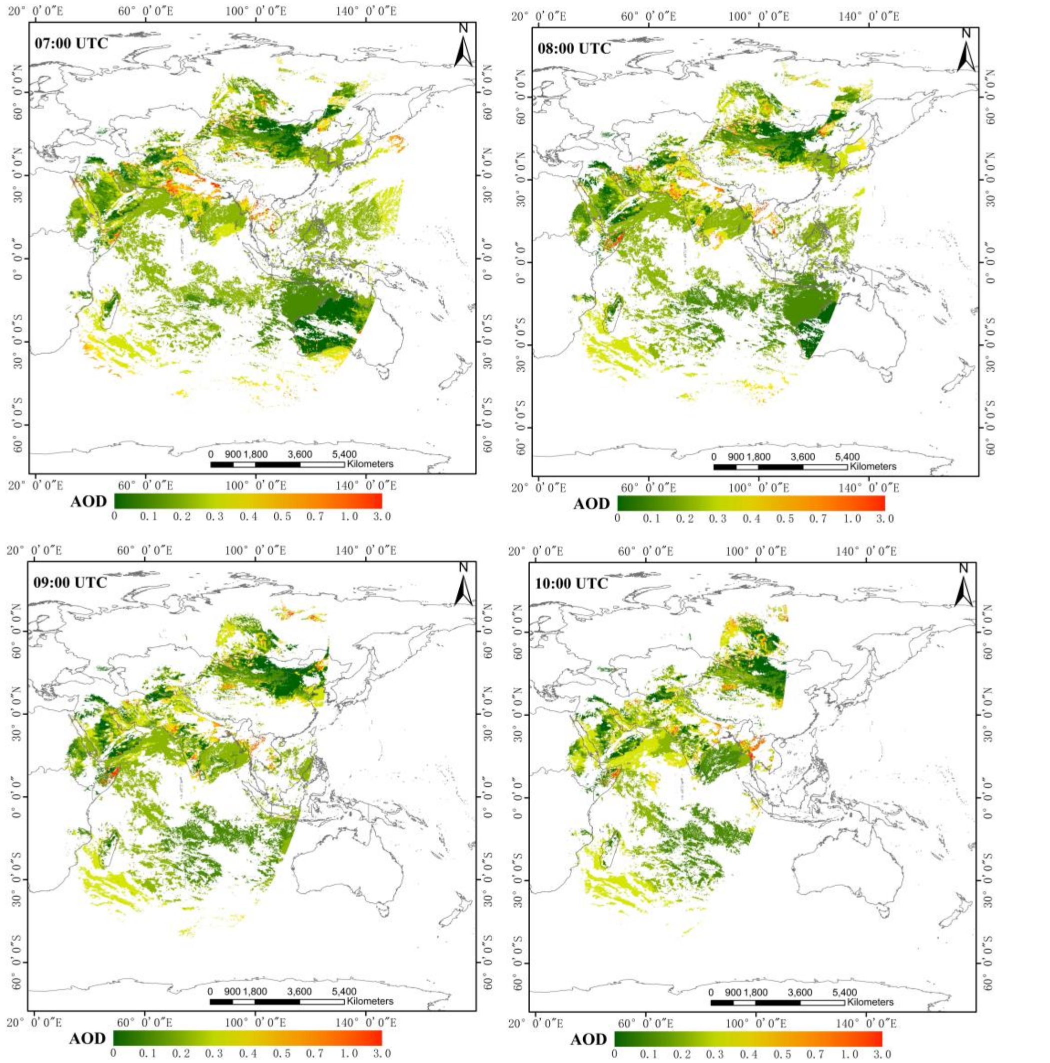

Figure 9. Hourly averaged spatial distributions of the AOD retrieved from FY-4A/AGRI data over the full disk using the NNAeroG algorithm, for each hour from 03:00 to 10:00 (UTC) on 23 April 2020. At 04:00 UTC, the area in the red dashed with dot is South Asia. At 05:00 UTC, the area in the red dashed is the land–sea boundary area in northwest Australia.

As shown for the land–sea boundary area marked with the red square in Figure 9 retrieved at 05:00 UTC, the AOD is different over land than over sea. There are barely enough marine samples for our training, therefore the training in marine areas is insufficient even though we used the sites on the coastline. In the area south of the Australian continent, although we only used "clear sky" in FY-4A/AGRI CLM products, elevated AOD due to cloud contamination is still observed. Furthermore, at 06:00 and 07:00 UTC, the AOD results over marine areas have overestimation such as the high latitude ocean area, which is in the south of Australia. The blank of ground-based sites over this area leads to under-training and low retrieval accuracy. Due to the lack of pure ocean site data for training, the precision of AOD retrieval of NNAeroG-FY4A at the sea–land boundary and over the ocean is poor. Therefore, the current AOD products over the ocean of NNAeroG-FY4A are not recommended.

From Figure 9, the spatial distribution of AOD is generally consistent with Figure 6 of Xie et al. [26] in the same area (red dash-dot in 04:00 UTC) and time. Both of us can reflect the high AOD value phenomenon in South Asia and we aim at the full disk AOD retrieval. Land and straw-burning activities led to high AOD values in South and Southeast Asia, reflecting the close relationship between regional air quality and human activities [48]. Due to the high temporal and spatial resolution of FY-4A/AGRI, continuous monitoring of full disk aerosol can be realized.

5.2. Comparison with Himawari-8 AOD

Figure 10 shows a comparison between the AOD retrieved using Himawari-8/AHI data, i.e., the Himawari-8/AHI official (JAXA) product (top line) and retrieved using the NNAeroG algorithm (Chen et al.) [25] (middle) and the AOD retrieved with the NNAeroG algorithm using FY-4A/AHI data (bottom). All three data sets were retrieved using observations on 23 April 2020 for each hour from 03:00 to 06:00 UTC (left to right).

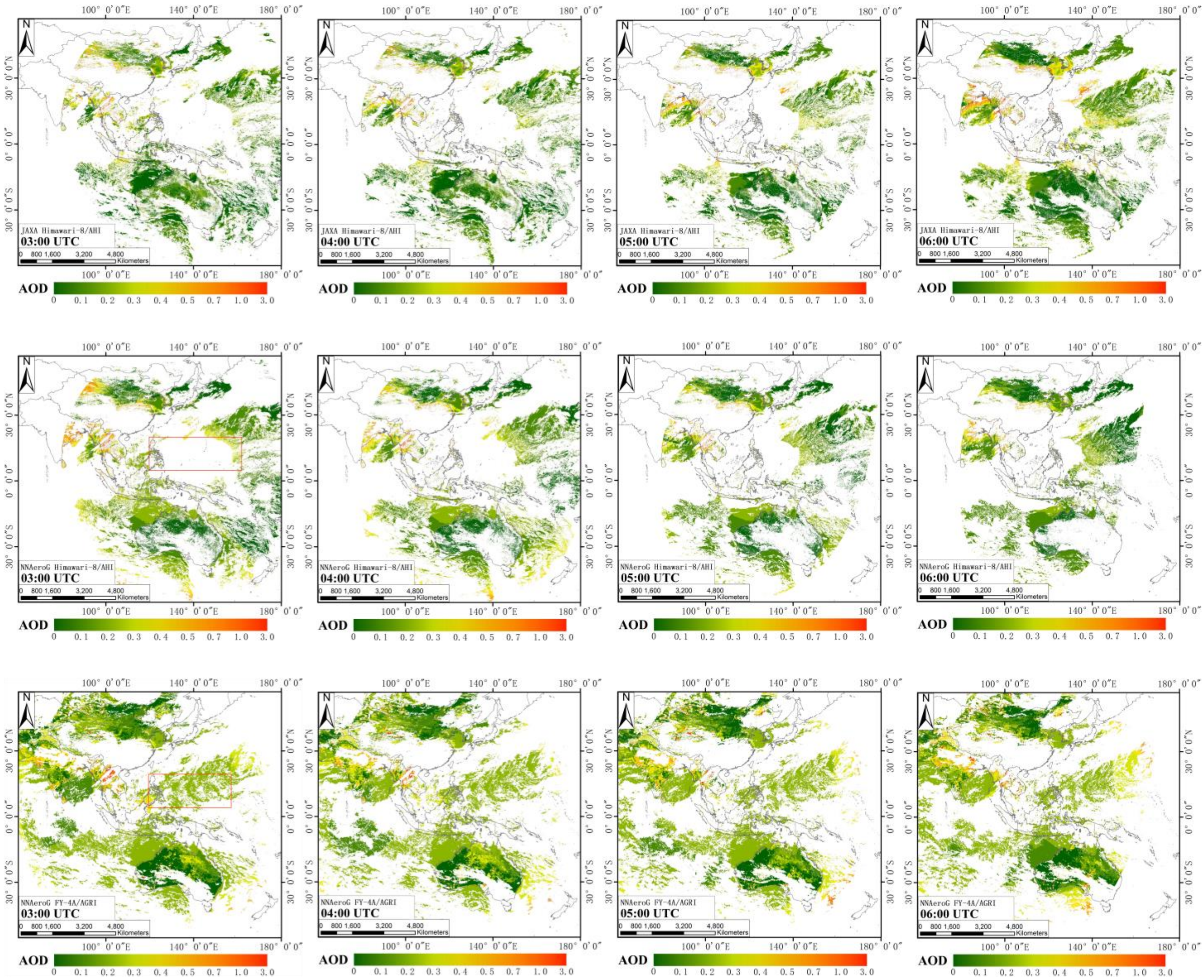

Figure 10. Hourly averaged spatial distributions of the AOD retrieved from Himawari-8/AHI and FY-4A/AGRI data over the full disk from 03:00 to 06:00 UTC on 23 April 2020. The first line is the Himawari-8/AHI AOD retrieval result obtained from the official JAXA product (Version 3.0), the second line is the Himawari-8/AHI AOD retrieval result that used the NNAeroG algorithm, and the third line is the FY-4A/AGRI AOD retrieval result that used the NNAeroG algorithm.

As shown in Figure 10, the spatial distribution of FY-4A/AGRI AOD is generally consistent with AHI AOD. In the second column, the spatial continuity of Himawari-8/AHI is not as good as that of FY-4A/AGRI. However, the FY-4A/AGRI CLM data are different from Himawari-8/AHI. FY-4A/AGRI AOD is affected by cloud mask data, especially in the Pacific area (30°N–10°S, 170°E–180°E). Himawari-8 has sun glint in this area, while FY-4A has not, which leads to different retrieval results in the same areas (red box area in 03:00 UTC NNAeroG FY-4A/AGRI and Himawari-8/AHI). In general, the AOD retrieval accuracy using the NNAeroG algorithm is higher than the Himawari-8/AHI official algorithm (from Table 4) [23,24], especially in spatial continuity.

5.3. Improvement Test over Arid Area

To analyze whether increasing the number of samples could improve the retrieval accuracy in arid areas, three sites' samples (Ieodo_Station (32.123°N, 125.182°E), Dongsha_Island (20.699°N, 116.729°E), REUNION_ST_DENIS (20.901°S, 55.485°E)) were copied and augmented by adding 2% Gaussian noise. The independent AOD validation results predicted by the retrained NNAeroG are shown in Figure 11.

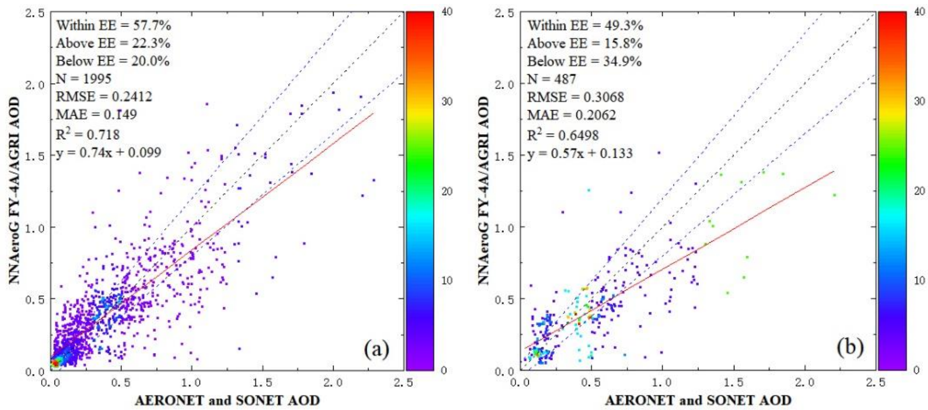

Figure 11. Scatterplots of the AOD retrieved using FY-4A/AGRI over full disk (**a**) and arid areas (**b**) versus AERONET and SONET reference data. The blue lines are the EE envelopes for AOD of ± (0.05 + 15%). The red line is the linear fitting line of AOD. The black line represents the 1:1 line.

Figure 11 shows the validation of the AOD retrieved using FY-4A/AGRI data with the arid-augmented NNAeroG algorithm. Over the arid areas, the values of the statistical metrics RMSE, MAE, R^2 and EE15 are 0.3068, 0.2062, 0.6498 and 49.3%, respectively. Although the AOD retrieval accuracy EE15 in arid areas was improved by 1.7% with arid sample augmentation, the EE15 of full disk retrieval accuracy was decreased by 1%. Only increasing samples through data expansion without obtaining more actual observations cannot achieve significant improvement.

6. Conclusions

The official AOD product of FY-4A/AGRI has not been released and the previous studies of FY-4A/AGRI AOD retrieval only focus on dark target areas which are not oriented to the full disk. In this paper, FY-4A/AGRI full disk AOD retrieval was realized for the first time since FY-4A was launched on 11 December 2016. FY-4A/AGRI has good AOD retrieval capability and it is worth further developing a comprehensive AOD retrieval algorithm. The algorithm of NNAeroG based on FCNN was used to retrieve AOD over the FY-4A/AGRI full disk area. The 4 km full disk FY-4A/AGRI data from 2017 to 2020, L1.5 AERONET data from 2017 to 2020 and L1.5 SONET data from 2017 to 2019 were collocated with the FY-4A/AGRI data for training, with part of the ground-based network data set aside as reference data set for independent validation. In NNAeroG, the RF method is used to optimize the features of FY-4A/AGRI spectral information and spatial information and screen the important input features. The NDVI and different spectral band data of Himawari-8/AHI were used in a modified version of NNAeroG. The algorithm is applied to retrieve AOD using FY-4A/AGRI data with a spatial resolution of 4 km and temporal resolution of 15 min to realize continuous aerosol monitoring throughout the day for the full disk.

(1) For independent validation, 58.7% of the AOD retrieved using the validation data are within EE15, the RMSE, MAE and R^2 are 0.237, 0.145 and 0.733, respectively. The AOD predicted by NNAeroG is consistent with the ground-based data generally;

(2) Over different surface types, the AOD is the best over vegetated areas and poor over arid and marine areas. The accuracy of AOD retrieval over vegetated, arid, and marine areas within EE15 are 66.7%, 47.6%, and 38.8%, respectively. Based on the NNAeroG test on FY-4A AOD retrieval, it was shown that NNAeroG has the ability for AOD retrieval. Over marine areas, there are barely any ocean sites and few effective observation data for neural network training. Furthermore, when the AOD of the ocean-atmosphere is less than 0.1, the satellite does not have enough aerosol optical signals to retrieve the AOD. Therefore, the current AOD products over the ocean of NNAeroG-FY4A/AGRI are not recommended. Further development of targeted algorithms for marine areas is expected to improve the full disk AOD retrieval accuracy. In the future, supplementary ocean satellite products for training would be considered;

(3) AOD retrieval is overestimated in the high latitude marine areas. The lack of ground-based sites over this area leads to under-training and low retrieval accuracy.

The accuracy of NNAeroG generally rises with the increase in the number of training sites (effective observation data), rather than the simple augmentation of the number of training samples. More ground-based data from AERONET and SONET sites or combined MISR or POLDER or future data sets from planned sensors with polarization can be used for higher accuracy AOD retrieval in the future.

Author Contributions: Conceptualization, H.D. and X.C.; methodology, H.D., X.C. and L.Z.; software, H.D., X.C., Y.Z. and L.Z.; validation, S.L., F.Z., J.L. (Jun Liu) and X.G.; formal analysis, L.Z., S.L., and J.L. (Jiaguo Li); investigation, X.C. and X.G.; resources, L.Z., L.S. and F.W.; data curation, L.Z. and Y.S.; writing—original draft preparation, H.D.; writing—review and editing, H.D., G.d.L. and X.C.; visualization, H.D. and G.d.L.; supervision, L.Z. and X.G. All authors have read and agreed to the published version of the manuscript.

Funding: This research was funded by the National Key Research and Development Program of China (Grant No. 2020YFE0200700 and Grant No. 2019YFE0126600) and the National Natural Science Foundation of China (Grant No. 42171342).

Data Availability Statement: Data used in the reported studies were obtained from websites as indicated in the text.

Acknowledgments: The authors acknowledge the Chinese Academy of Meteorological Sciences, the Chinese Academy of Meteorological Sciences, SONET and AERONET groups for the satellite and ground-based data, and the Himawari-8/AHI data system (P-Tree).

Conflicts of Interest: The authors declare no conflict of interest. The funders had no role in the design of the study; in the collection, analyses, or interpretation of data; in the writing of the manuscript, or in the decision to publish the results.

References

1. Kaufman, Y.J.; Tanré, D.; Gordon, H.R.; Nakajima, T.; Lenoble, J.; Frouin, R.; Grassl, H.; Herman, B.M.; King, M.D.; Teillet, P.M. Passive remote sensing of tropospheric aerosol and atmospheric correction for the aerosol effect. *J. Geophys. Res. Atmos.* **1997**, *102*, 16815–16830. [CrossRef]
2. Yu, L.; Zhang, M.; Wang, L.; Lu, Y.; Li, J. Effects of aerosols and water vapour on spatial-temporal variations of the clear-sky surface solar radiation in China. *Atmos. Res.* **2021**, *248*, 16. [CrossRef]
3. Qin, K.; Wang, L.; Wu, L.; Xu, J.; Rao, L.; Letu, H.; Shi, T.; Wang, R. A campaign for investigating aerosol optical properties during winter hazes over Shijiazhuang, China. *Atmos. Res.* **2017**, *198*, 113–122. [CrossRef]
4. Holben, B.N.; Eck, T.F.; Slutsker, I.; Tanre, D.; Buis, J.P.; Setzer, A.; Vermote, E.; Reagan, J.A.; Kaufman, Y.J.; Nakajima, T.; et al. AERONET—A federated instrument network and data archive for aerosol characterization. *Remote Sens. Environ.* **1998**, *66*, 1–16. [CrossRef]
5. Li, Z.; Gu, X.; Wang, L.; Li, D.; Xie, Y.; Li, K.; Dubovik, O.; Schuster, G.; Goloub, P.; Zhang, Y.; et al. Aerosol physical and chemical properties retrieved from ground-based remote sensing measurements during heavy haze days in Beijing winter. *Atmos. Chem. Phys.* **2013**, *13*, 10171–10183. [CrossRef]

6. Ningombam, S.S.; Larson, E.J.L.; Dumka, U.C.; Estellés, V.; Campanelli, M.; Steve, C. Long-term (1995–2018) aerosol optical depth derived using ground based AERONET and SKYNET measurements from aerosol aged-background sites. *Atmos. Pollut. Res.* **2019**, *10*, 608–620. [CrossRef]
7. Che, H.; Xia, X.; Zhao, H.; Dubovik, O.; Holben, B.N.; Goloub, P.; Cuevas-Agulló, E.; Estelles, V.; Wang, Y.; Zhu, J.; et al. Spatial distribution of aerosol microphysical and optical properties and direct radiative effect from the China Aerosol Remote Sensing Network. *Atmos. Chem. Phys.* **2019**, *19*, 11843–11864. [CrossRef]
8. Hair, J.W.; Hostetler, C.A.; Cook, A.L.; Harper, D.B.; Ferrare, R.A.; Mack, T.L.; Welch, W.; Isquierdo, L.R.; Hovis, F.E. Airborne high spectral resolution lidar for profiling aerosol optical properties. *Appl. Opt.* **2008**, *47*, 6734–6752. [CrossRef]
9. Burton, S.P.; Ferrare, R.A.; Hostetler, C.A.; Hair, J.W.; Rogers, R.R.; Obland, M.D.; Butler, C.F.; Cook, A.L.; Harper, D.B.; Froyd, K.D. Aerosol classification using airborne high spectral resolution LiDAR measurements–methodology and examples. *Atmos. Meas. Tech.* **2012**, *5*, 73–98. [CrossRef]
10. Levy, R.C.; Mattoo, S.; Munchak, L.A.; Remer, L.A.; Sayer, A.M.; Patadia, F.; Hsu, N.C. The collection 6 MODIS aerosol products over land and ocean. *Atmos. Meas. Tech.* **2013**, *6*, 2989–3034. [CrossRef]
11. Kolmonen, P.; Sogacheva, L.; Virtanen, T.H.; de Leeuw, G.; Kulmala, M. The ADV/ASV AATSR aerosol retrieval algorithm: Current status and presentation of a full-mission AOD datase. *Int. J. Digit. Earth* **2016**, *9*, 545–561. [CrossRef]
12. Che, H.; Gui, K.; Xia, X.; Wang, Y.; Holben, B.N.; Goloub, P.; Cuevas-Agulló, E.; Wang, H.; Zheng, Y.; Zhao, H.; et al. Large contribution of meteorological factors to inter-decadal changes in regional aerosol optical depth. *Atmos. Chem. Phys.* **2019**, *19*, 10497–10523. [CrossRef]
13. She, L.; Xue, Y.; Yang, X.; Leys, J.; Guang, J.; Che, Y.; Fan, C.; Xie, Y.; Li, Y. Joint retrieval of aerosol optical depth and surface reflectance over land using geostationary satellite data. *IEEE Trans. Geosci. Remote Sens.* **2019**, *57*, 1489–1501. [CrossRef]
14. Yang, F.; Wang, Y.; Tao, J.; Wang, Z.; Fan, M.; de Leeuw, G.; Chen, L. Preliminary investigation of a new AHI aerosol optical depth (AOD) retrieval algorithm and evaluation with multiple source AOD measurements in China. *Remote Sens.* **2018**, *10*, 748. [CrossRef]
15. Li, L.; Dubovik, O.; Derimian, Y.; Schuster, G.L.; Lapyonok, T.; Litvinov, P.; Ducos, F.; Fuertes, D.; Chen, C.; Li, Z.; et al. Retrieval of aerosol components directly from satellite and ground-based measurements. *Atmos. Chem. Phys.* **2019**, *19*, 13409–13443. [CrossRef]
16. Li, L.; Che, H.; Zhang, X.; Chen, C.; Chen, X.; Gui, K.; Liang, Y.; Wang, F.; Derimian, Y.; Fuertes, D.; et al. A satellite-measured view of aerosol component content and optical property in a haze-polluted case over North China Plain. *Atmos. Res.* **2022**, *266*, 105958. [CrossRef]
17. Li, L.; Derimian, Y.; Chen, C.; Zhang, X.; Che, H.; Schuster, G.L.; Fuertes, D.; Litvinov, P.; Lapyonok, T.; Lopatin, A.; et al. Climatology of aerosol component concentrations derived from multi-angular polarimetric POLDER-3 observations using GRASP algorithm. *Earth Syst. Sci. Data* **2022**, *14*, 3439–3469. [CrossRef]
18. de Leeuw, G.; Holzer-Popp, T.; Bevan, S.; Davies, W.H.; Descloitres, J.; Grainger, R.G.; Griesfeller, J.; Heckel, A.; Kinne, S.; Klüser, L.; et al. Evaluation of seven European aerosol optical depth retrieval algorithms for climate analysis. *Remote Sens. Environ.* **2015**, *162*, 295–315. [CrossRef]
19. Yoshida, M.; Kikuchi, M.; Nagao, T.M.; Murakami, H.; Nomaki, T.; Higurashi, A. Common retrieval of aerosol properties for imaging satellite sensors. *J. Meteorol. Soc. Jpn. Ser. II* **2018**, *96B*, 193–209. [CrossRef]
20. Ge, B.; Li, Z.; Liu, L.; Yang, L.; Chen, X.; Hou, W.; Zhang, Y.; Li, D.; Li, L.; Qie, L. A Dark Target Method for Himawari-8/AHI Aerosol Retrieval: Application and Validation. *IEEE Trans. Geosci. Remote Sens.* **2019**, *57*, 381–393. [CrossRef]
21. Li, D.; Qin, K.; Wu, L.; Mei, L.; de Leeuw, G.; Xue, Y.; Shi, Y.; Li, Y. Himawari-8-Derived Aerosol Optical Depth Using an Improved Time Series Algorithm Over Eastern China. *Remote Sens.* **2020**, *12*, 978. [CrossRef]
22. Wang, L.; Yu, C.; Cai, K.; Zheng, F.; Li, S. Retrieval of Aerosol Optical Depth from the Himawari-8 Advanced Himawari Imager data: Application over Beijing in the summer of 2016. *Atmos. Environ.* **2020**, *241*, 117788. [CrossRef]
23. She, L.; Zhang, H.K.; Li, Z.; de Leeuw, G.; Huang, B. Himawari-8 Aerosol Optical Depth (AOD) Retrieval Using a Deep Neural Network Trained Using AERONET Observations. *Remote Sens.* **2020**, *12*, 4125. [CrossRef]
24. Chen, X.; Zhao, L.; Zheng, F.; Li, J.; Li, L.; Ding, H.; Zhang, K.; Liu, S.; Li, D.; de Leeuw, G. Neural Network AEROsol Retrieval for Geostationary Satellite (NNAeroG) Based on Temporal, Spatial and Spectral Measurements. *Remote Sens.* **2022**, *14*, 980. [CrossRef]
25. Jiang, X.; Xue, Y.; Jin, C.; Bai, R.; Li, N.; Sun, Y. Retrieval of Aerosol Optical Depth Over Land Using Fy-4Aagri Geostationary Satellite Data. In Proceedings of the 2021 IEEE International Geoscience and Remote Sensing Symposium (IGARSS), Brussels, Belgium, 11–16 July 2021; pp. 1931–1934.
26. Xie, Y.; Li, Z.; Guang, J.; Hou, W.; Salam, A.; Ali, Z.; Fang, L. Aerosol Optical Depth Retrieval Over South Asia Using FY-4A/AGRI Data. *IEEE Trans. Geosci. Remote Sens.* **2022**, *60*, 4104814. [CrossRef]
27. Chen, X.; de Leeuw, G.; Arola, A.; Liu, S.; Liu, Y.; Li, Z.; Zhang, K. Joint retrieval of the aerosol fine mode fraction and optical depth using MODIS spectral reflectance over northern and eastern China: Artificial neural network method. *Remote Sens. Environ.* **2020**, *249*, 112006. [CrossRef]
28. Holben, B.N.; Tanré, D.; Smirnov, A.; Eck, T.F.; Slutsker, I.; Abuhassan, N.; Newcomb, W.W.; Schafer, J.S.; Chatenet, B.; Lavenu, F.; et al. An emerging ground-based aerosol climatology: Aerosol optical depth from AERONET. *J. Geophys. Res. Atmos.* **2001**, *106*, 12067–12097. [CrossRef]

29. Li, Z.Q.; Xu, H.; Li, K.T.; Li, D.H.; Xie, Y.S.; Li, L.; Zhang, Y.; Gu, X.F.; Zhao, W.; Tian, Q.J.; et al. Comprehensive study of optical, physical, chemical, and radiative properties of total columnar atmospheric aerosols over China: An overview of sun–sky radiometer observation network (SONET) measurements. *Bull. Am. Meteorol. Soc.* **2018**, *99*, 739–755. [CrossRef]
30. Yang, J.; Zhang, Z.; Wei, C.; Lu, F.; Guo, Q. Introducing the new generation of Chinese geostationary weather satellites, Fengyun-4. *Bull. Am. Meteorol. Soc.* **2017**, *98*, 1637–1658. [CrossRef]
31. Wang, G.; Jiang, L.; Liu, X.; Cui, H.; Yang, J.; Wang, J. Estimation of Fractional Snow Cover From Fy-4a/Agri. In Proceedings of the 2019 IEEE International Geoscience and Remote Sensing Symposium (IGARSS), Yokohama, Japan, 28 July–2 August 2019; pp. 4064–4067.
32. Qiao, H.; Zhang, P.; Li, Z.; Liu, C. A New Geostationary Satellite-Based Snow Cover Recognition Method for FY-4A AGRI. *IEEE Trans. Geosci. Remote Sens.* **2021**, *14*, 11372–11385. [CrossRef]
33. Tan, Z.; Ma, S.; Zhao, X.; Yan, W.; Lu, W. Evaluation of Cloud Top Height Retrievals from China's Next-Generation Geostationary Meteorological Satellite FY-4A. *J. Meteorol. Res.* **2019**, *33*, 553–562. [CrossRef]
34. Lu, F.; Zhang, X.; Chen, B.; Liu, H.; Wu, R.; Han, Q.; Feng, X.; Li, Y.; Zhang, Z. FY-4 geostationary meteorological satellite imaging characteristics and its application prospects. *J. Mar. Meteorol.* **2017**, *37*, 1–12.
35. Eck, T.F.; Holben, B.N.; Reid, J.S.; Dubovik, O.; Smirnov, A.; O'Neill, N.T.; Slutsker, I.; Kinne, S. Wavelength dependence of the optical depth of biomass burning, urban, and desert dust aerosols. *J. Geophys. Res.* **1999**, *104*, 31333–31349. [CrossRef]
36. Giles, D.M.; Sinyuk, A.; Sorokin, M.G.; Schafer, J.S.; Smirnov, A.; Slutsker, I.; Eck, T.F.; Holben, B.N.; Lewis, J.R.; Campbell, J.R.; et al. Advancements in the aerosol robotic network (AERONET) version 3 database–automated near-real-time quality control algorithm with improved cloud screening for sun photometer aerosol optical depth (AOD) measurements. *Atmos. Meas. Tech.* **2019**, *12*, 169–209. [CrossRef]
37. Li, Z.; Li, D.; Li, K.; Xu, H.; Chen, X.; Chen, C.; Xie, Y.; Li, L.; Li, L.; Li, W.; et al. Sun-sky radiometer observation network with the extension of multi-wavelength polarization measurements. *J. Remote Sens.* **2015**, *19*, 495–519.
38. Xie, Y.; Li, Z.; Li, D.; Xu, H.; Li, K. Aerosol Optical and Microphysical Properties of Four Typical Sites of SONET in China Based on Remote Sensing Measurements. *Remote Sens.* **2015**, *7*, 9928–9953. [CrossRef]
39. Yan, X.; Liang, C.; Jiang, Y.; Luo, N.; Zang, Z.; Li, Z. A deep learning approach to improve the retrieval of temperature and humidity profiles from a ground-based microwave radiometer. *IEEE Trans. Geosci. Remote Sens.* **2020**, *58*, 842–8437. [CrossRef]
40. Glorot, X.; Bordes, A.; Bengio, Y. Deep sparse rectifier neural networks. In Proceedings of the Fourteenth International Conference on Artificial Intelligence and Statistics, Fort Lauderdale, FL, USA, 11–13 April 2011; pp. 315–323.
41. Levy, R.C.; Remer, L.A.; Kleidman, R.G.; Mattoo, S.; Ichoku, C.; Kahn, R.; Eck, T.F. Global evaluation of the Collection 5 MODIS dark-target aerosol products over land. *Atmos. Chem. Phys.* **2010**, *10*, 10399–10420. [CrossRef]
42. Xiao, Q.; Zhang, H.; Choi, M.; Li, S.; Kondragunta, S.; Kim, J.; Holben, B.; Levy, R.C.; Liu, Y. Evaluation of VIIRS, GOCI, and MODIS Collection 6 AOD retrievals against ground sunphotometer observations over East Asia. *Atmos. Chem. Phys.* **2016**, *16*, 1255–1269. [CrossRef]
43. Wang, X.; Min, M.; Wang, F.; Guo, J.; Li, B.; Tang, S. Intercomparisons of Cloud Mask Products Among Fengyun-4A, Himawari-8, and MODIS. *IEEE Trans. Geosci. Remote Sens.* **2019**, *57*, 8827–8839. [CrossRef]
44. Zhang, P.; Zhu, L.; Tang, S.; Gao, L.; Chen, L.; Zheng, W.; Han, X.; Chen, J.; Shao, J. General Comparison of FY-4A/AGRI With Other GEO/LEO Instruments and Its Potential and Challenges in Non-meteorological Applications. *Front. Earth Sci.* **2019**, *6*, 224. [CrossRef]
45. Tian, X.; Sun, L. Retrieval of Aerosol Optical Depth over Arid Areas from MODIS Data. *Atmosphere* **2016**, *7*, 134. [CrossRef]
46. Wang, Y.; Wang, J.; Levy, R.C.; Xu, X.; Reid, J.S. MODIS Retrieval of Aerosol Optical Depth over Turbid Coastal Water. *Remote Sens.* **2017**, *9*, 595. [CrossRef] [PubMed]
47. Wang, Y.; Wang, J.; Levy, R.C.; Shi, Y.R.; Mattoo, S.; Reid, J.S. First retrieval of AOD at fine resolution over shallow and turbid coastal waters from MODIS. *Geophys. Res. Lett.* **2021**, *48*, e2021GL094344. [CrossRef]
48. Lin, M.; Begho, T. Crop residue burning in South Asia: A review of the scale, effect, and solutions with a focus on reducing reactive nitrogen losses. *J. Environ. Manag.* **2022**, *314*, 115104. [CrossRef]